NASA TECHNICAL NOTE

NASA TN D-2534

A RADIATION CLIMATOLOGY IN THE VISIBLE AND INFRARED FROM THE TIROS METEOROLOGICAL SATELLITES

by W. R. Bandeen, M. Halev, and I. Strange

Goddard Space Flight Center
Greenbelt, Md.

NATIONAL AERONAUTICS AND SPACE ADMINISTRATION • WASHINGTON, D. C. • JUNE 1965

A RADIATION CLIMATOLOGY IN THE VISIBLE AND INFRARED FROM THE TIROS METEOROLOGICAL SATELLITES

By W. R. Bandeen, M. Halev, and I. Strange

Goddard Space Flight Center
Greenbelt, Md.

NATIONAL AERONAUTICS AND SPACE ADMINISTRATION

For sale by the Clearinghouse for Federal Scientific and Technical Information
Springfield, Virginia 22151 – Price $2.00

A RADIATION CLIMATOLOGY IN THE VISIBLE AND INFRARED FROM THE TIROS METEOROLOGICAL SATELLITES

by
W. R. Bandeen, M. Halev, I. Strange
Goddard Space Flight Center

SUMMARY

Radiometric measurements in the visible and infrared have been made intermittently since 1960 by the meteorological satellites, Tiros II, III, IV, and VII. Measurements of reflected solar radiation have been acquired within filtered passbands of approximately 0.2-6 μ and 0.55-0.75 μ and, of emitted long wave radiation, within passbands of approximately 8-12μ, 8-30μ, 6-6.5μ, and 14.8-15.5μ. Tiros VII has acquired continuous radiometric data over the earth for more than a year, increasing significantly the potential of its data for climatological studies, as compared to the earlier experiments of shorter duration.

A limited climatology of the spatial and temporal variations of the total outgoing long wave radiation and of the planetary albedo is derived from the essentially beam measurements within the 5° field of view of the Tiros VII five-channel, scanning radiometer. The results essentially agree with previous studies of the planetary heat balance, based on conventional data, but several interesting differences appear. The satellite data indicate a disproportionately high emission of radiation from the subtropical anticyclones, while the meridional gradient of the mean zonal albedo is larger than indicated in several recent studies.

In addition, the relative planetary distribution of atmospheric moisture is inferred from measurements within the 6.3μ band of water vapor, and the seasonal changes of mean temperatures in the stratosphere between about 15 and 35 km are shown from measurements within the 15μ band of CO_2.

CONTENTS

A RADIATION CLIMATOLOGY IN THE VISIBLE AND INFRARED FROM THE TIROS METEOROLOGICAL SATELLITES*

by
W. R. Bandeen, M. Halev, I. Strange
Goddard Space Flight Center

INTRODUCTION

Climatological investigations by means of radiation data from the Tiros meteorological satellites have been hindered, at least in part, by the relatively short lifetimes of the early experiments flown on Tiros II, III, and IV. The medium-resolution scanning radiometer flown on Tiros VII, however, has acquired continuous data over the earth for more than one year, increasing significantly the potential value of the radiometric measurements for climatological studies.

The design of the radiometers, their calibration, the information flow, and the data reduction techniques have been described previously (References 1 - 3), as have the physical significance of the experiment and its synoptic use potential (References 4 - 6). In this paper we shall discuss three climatological applications of radiation data from Tiros VII, and from Tiros IV for one type of measurement (in the 6.3μ H_2O band) that was not made by Tiros VII.

The radiometer measures essentially beam radiation within a 5° field-of-view from five channels, each made sensitive to a different part of the spectrum by means of filters and other optical elements. The nominal wavelength limits of the sensors flown on the various satellites are shown in Table 1.

CALIBRATION

The calibration of the infrared channels is carried out in the laboratory by viewing a blackbody cavity, and the primary calibrated quantity is the "equivalent blackbody temperature, $T_{BB}(°K)$ ". It follows that the "effective radiant emittance, $\bar{W}$ (watts m^{-2})" and the "effective radiance, $\bar{N}$ (watts m^{-2} $ster^{-1}$)" to which a sensor responds are given by

$$\bar{W} = \pi\bar{N} = \int_{\lambda=0}^{\infty} W_\lambda \left(T_{BB}\right) \phi_\lambda \, d\lambda \, , \qquad (1)$$

*Presented at the International Radiation Symposium, International Association of Meteorology and Atmospheric Physics (I.U.G.G.), Leningrad, August 1964.

Table 1

Nominal Wavelength Intervals of Tiros Radiometers.

Nominal Wavelength Interval	Satellite			
	Tiros II	Tiros III	Tiros IV*	Tiros VII**
6-6.5 μ (H_2O absorption)	X(1)	X(1)	X(5)	
8-12 μ (atmospheric window)	X(5)	X(2)	X(5)	X
8-30 μ (long-wave radiation)	X(1)	X(1)		X
14.8-15.5 μ (CO_2 absorption)				X
0.2-6 μ (reflected solar radiation)	X(0)	X(2)	X(5)	X
0.55-0.75 μ (reflected solar radiation in the visible)	X(0)	X(1)	X(5)	X

*Only four channels were used on Tiros IV. The (X's) indicate the channels which were included on each radiometer, and the parenthetical numbers indicate the approximate number of months of usable data.

**The radiometer on Tiros VII, launched June 19, 1963, is still operating as of this writing. Detailed characteristics of all experiments are found in their respective Users' Manuals (References 7-10).

where $W_\lambda(T_{BB})$ is the spectral radiant emittance from a blackbody at temperature T_{BB} (i.e., Planck radiation) and ϕ_λ is the effective spectral response function for the particular channel. The constant π transforms Planck radiance (intensity) to blackbody radiant emittance (flux).

The calibration of the short-wave channels is carried out in the laboratory by viewing a diffuse sheet of white paper of known spectral reflectivity, ρ_λ, illuminated at normal incidence by a standard lamp of known spectral radiant intensity, J_λ (watts ster^{-1} micron^{-1}), at a known distance R (meters). The reflectance of the white paper is *assumed* to be ideally diffuse (i.e., Lambertian). The effective radiant emittance and radiance to which a sensor responds, then, are

$$\bar{W} = \pi\bar{N} = \frac{1}{R^2}\int_{\lambda=0}^{\infty} J_\lambda\,\rho_\lambda\,\phi_\lambda\,d\lambda\,. \qquad (2)$$

In order to interpret the short-wave measurements in terms of reflectance of solar radiation from the earth and atmosphere, one must know the "effective solar constant, $\bar{W}^*$ (watts m^{-2})", i.e., the measurement which would result if the radiometer field-of-view were completely filled by an ideally diffuse reflector of unit reflectivity when illuminated by one solar constant at normal incidence, expressed by

$$\bar{W}^* = \int_0^{\infty} S_\lambda\,\phi_\lambda\,d\lambda\,, \qquad (3)$$

where S_λ is the spectral irradiance of the earth by the sun at unit distance. The solar constant

$$\int_0^{\infty} S_\lambda\,d\lambda = 1395 \text{ watts m}^{-2} = 2.0 \text{ gm cal cm}^{-2}\text{ min}^{-1}.$$

The reflectance of solar radiation, r_0, assuming that the reflectance is *independent of wavelength* and that the radiation is *reflected isotropically* is given by

$$r_0 = \frac{\overline{W}}{\overline{W}^* \cos \zeta} R_a^2 , \tag{4}$$

where ζ is the solar zenith angle and R_a is the distance of the earth from the sun in astronomical units. Equation 4 was used to calculate reflectance (and, assuming isotropy, albedos) in this paper, although there is evidence that appreciable errors may result if the angular dependence of the backscattered radiation is not included*. The maximum allowable solar zenith angle, to insure adequate illumination, was $\zeta = 70°$.

THE PLANETARY HEAT BALANCE

We shall investigate only the heat balance at the top of the atmosphere, and not consider the more complicated study of the heat budget of the atmosphere alone, at this time. In our study we shall use data obtained over a full year from Tiros VII. A number of problems have arisen concerning the interpretation and treatment of the satellite data. We shall discuss the most important of these below.

Coverage

The orbit of Tiros VII is nearly circular, at a mean height of 635 km, and inclined to the equator by 58°. For this reason, the polar regions cannot be observed (Figure 1). The maximum allowable angle of the sensor optical axis from the nadir (the "nadir angle") was 45° for data to be accepted. Therefore, the coverage was extended beyond the subsatellite track to latitudes 63.5°N. and S. For our purposes this broad zone of coverage, which includes 89.5% of the world's surface area, shall be termed the "quasi-globe." The two "V-shaped" gaps near Asia and South America (Figure 1) result from the combined constraints of the location of the three Command and Data Acquisition Stations in the United States and the limit of the storage capacity of the satellite tape recorder to one orbit of data. In addition, there is a temporal coverage problem. Because of the orbital regression and the motion of the sun, a period of 76 days (the "orbital synodic cycle") is required for the orbital nodes to move through one complete cycle relative to the sun and, hence, for all latitudes to be sampled at all local times. Figure 2 shows the heliocentric views of the Tiros VII orbit at launch and at four quarters throughout a 76-day cycle.

Selection of Spectral Intervals

Ideally the best inference of total long-wave radiation should derive from measurements by the 8-30 micron channel and the best inference of total reflected solar radiation should derive

*A. Arking discussed this point in a paper presented at the Symposium on Atmospheric Radiation sponsored by the Radiation Commission of the International Association of Meteorology and Atmospheric Physics (I.U.G.G.) at Leningrad, U.S.S.R. in August, 1964.

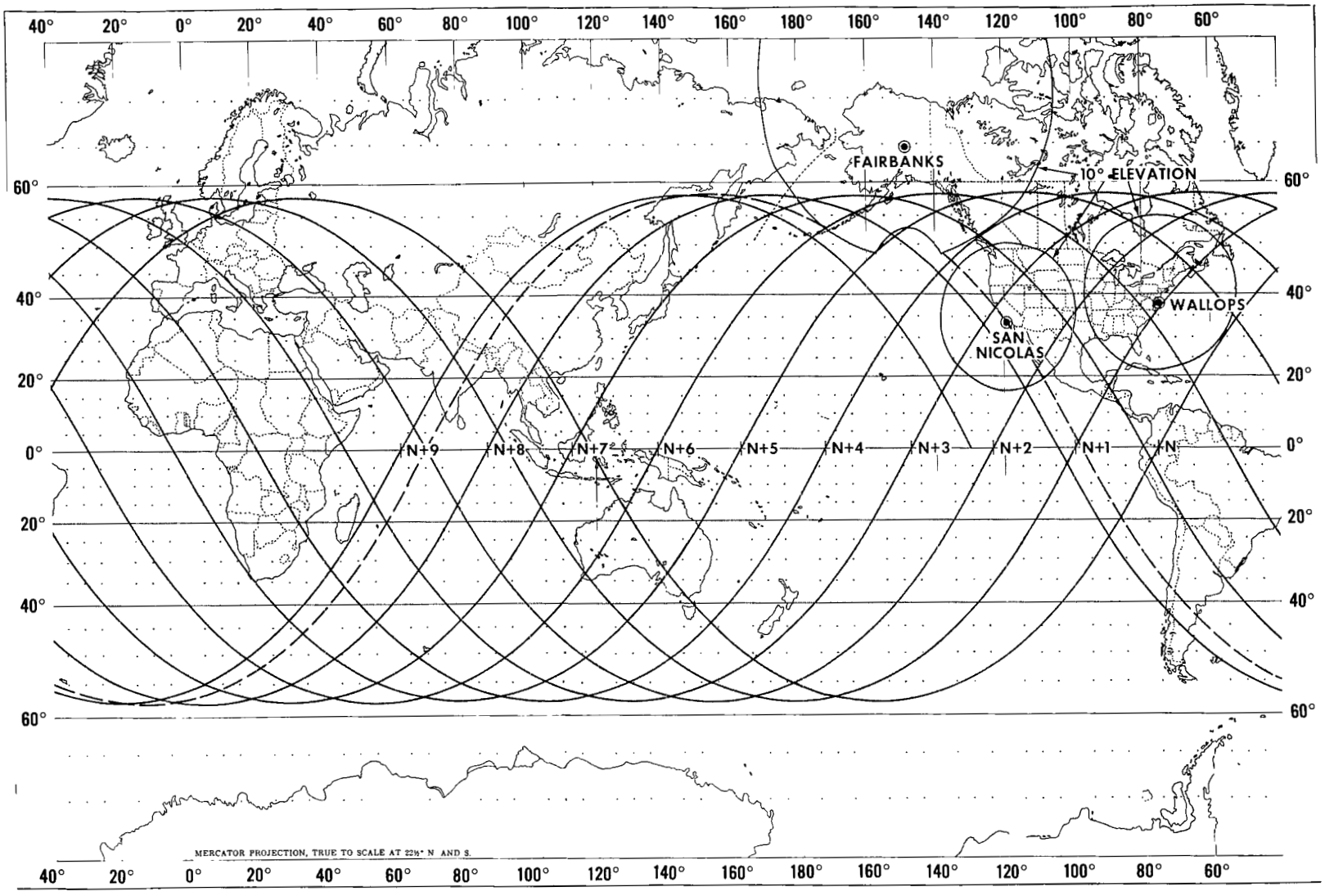

Figure 1—Nominal world-wide radiation data coverage for the Tiros VII satellite.

from measurements by the 0.2-6 micron channel. However, because of engineering problems and the long-term stability of the sensors, it was decided to use the 8-12 micron and 0.55-0.75 micron channels instead (cf. Reference 10).

Method of Converting T_{BB} Measurements to Total Outgoing Long-Wave Flux W

The method of Wark, Yamamoto, and Lienesch (Reference 11) was adopted for converting the beam measurements of the 8-12 micron channel to total outgoing flux. Plots of W vs. T_{BB} (and $\overline{W}$) calculated for three zenith angles are shown in Figure 3. The linear fit W, in langleys/minute, is

$$W\,(\text{ly min}^{-1}) = 0.141 + 0.00907\ \overline{W}\ (\text{watts m}^{-2}), \tag{5}$$

and was adopted for manually applying second-order corrections for observed degradation in the instrumental response to the data printed out by an electronic computer (cf. "Data Processing and Degradation of the Instrumental Response" below).

Modification Factor for Limb Darkening

The theoretical limb darkening contained in the work of Wark et al. (Reference 11) was determined under ideal conditions of either completely clear or completely overcast skies. The actual

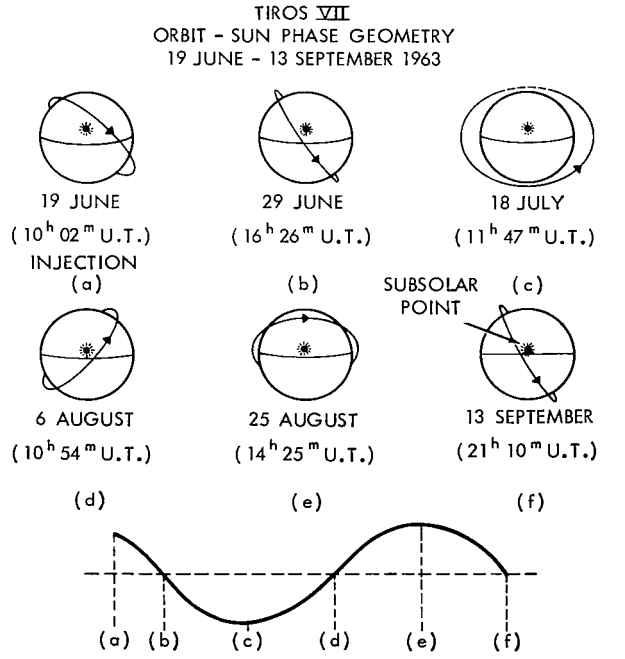

Figure 2—Heliocentric views of the Tiros VII orbit, illustrating the 76-day orbital synodic cycle. The sinusoid shows the convention for indicating the orbit-sun phase geometry in Figures 5 and 6.

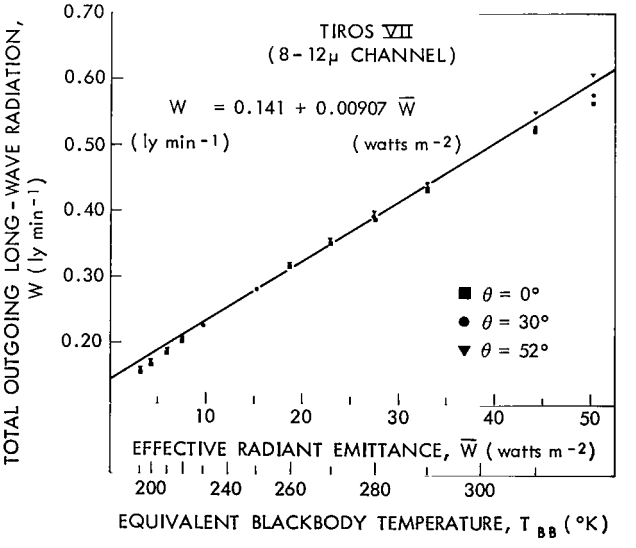

Figure 3—Total outgoing long-wave radiation as a function of equivalent blackbody temperature (and effective radiant emittance) for the 8-12μ channel of Tiros VII for three zenith angles, θ. The straight line approximation was adopted for applying corrections for observed instrumental degradation.

limb darkening was investigated using a two-dimensional distribution matrix containing 30 increments of radiance and 10 increments of zenith angle. The curve shown in Figure 4 was developed from the 50th percentile value of radiance in each of the zenith angle increments (after correcting for instrumental degradation; cf. Tiros IV Catalog-Manual: Reference 9), calculated by a computer from nearly 1.3×10^6 measurements by the 8-12 micron channel of Tiros IV. The corresponding theoretical limb darkening, calculated for the same vertical outgoing radiance, i.e., $\bar{N}(T_{BB} = 268.18^\circ K)$, is noticeably less in Figure 4. The ratio of the integral incorporating the empirical curve to that incorporating the theoretical curve, calculating the total fluxes from an arbitrary radiance measurement, N', at an average zenith angle, $\theta_{ave} = 35.5^\circ$, yielded the value

$$\frac{W_{EMPIRICAL}}{W_{THEORETICAL}} = \frac{\frac{N'}{E(\theta = 35.5^\circ)} \int_0^{\pi/2} E(\theta) \sin\theta\cos\theta\, d\theta}{\frac{N'}{T(\theta = 35.5^\circ)} \int_0^{\pi/2} T(\theta) \sin\theta\cos\theta\, d\theta} = 0.986 , \qquad (6)$$

where $E(\theta) = [N(\theta)/N(0)]_{EMPIRICAL}$ and $T(\theta) = [N(\theta)/N(0)]_{THEORETICAL}$. Values of total flux calculated by the computer, then, were reduced by the factor 0.986 as a first approximation to correct for the greater observed limb effects compared to the theoretically determined limb darkening.

Data Processing and Degradation of the Instrumental Response

An electronic computer was employed to process the data contained on magnetic tape (Final Meteorological Radiation Tapes, FMRT; cf. Tiros VII Catalog-Manual: Reference 10) to a grid print map format (cf. Reference 12). Briefly, a square-mesh grid containing 2376 elements was superimposed on a Mercator map base of the quasi-globe, and measurements were accumulated in appropriate grid squares by the computer over a period of about seven days. Then averages of all measurements in each grid square were taken resulting in a weekly map of data. In producing the weekly map the computer also calculated and printed out the average of all individual measurements processed (the "map average").

In Figure 5, the effective radiant emittances, $\bar{W}$, calculated by means of Equation 5 from the map average values of total outgoing long-wave flux, are shown for each of 19 weekly periods during the first year of Tiros VII (dots with bars). The 19 periods are numbered along the upper abscissa, and the sinusoid indicates the orbit-sun phase geometry (cf. Figure 2). The Roman numerals at the top of the figure indicate the calendar months making up the four seasons, each of which is represented by averages of data from four weekly periods, equally spaced every 19 days over a 76-day synodic cycle. The lengths of the bars indicate the number of days making up the data period, usually seven. A least-squares quadratic curve is shown for the map averages. The decrease with time is interpreted as indicating a degradation in the response of the instrument while in orbit. There are unavoidable gaps in the quasi-global coverage, caused by such factors as noise and engineering considerations preventing the successful acquisition and reduction of every possible orbit, which might bias the quasi-global map averages. Upon close examination

of the data, such biases were ascertained in the map averages of Figure 5. Therefore, values of $\bar{W}$ were calculated by means of Equation 5 for averages of the data over an equatorial region of the Pacific Ocean which was uniformly covered by all 19 weekly maps. The squares in Figure 5 refer to these values. A least-squares quadratic fit for the Pacific Ocean averages is shown in Figure 5 (top curve), and was adopted as representing the true instrumental degradation. Based upon this curve, then, correction factors, $h_2(t)$, were calculated to correct for degradation in the instrumental response. Because of the linear response characteristic of the radiometer, a degradation-corrected value, $\bar{W}'$, can be expressed by

$$\bar{W}' = h_2(t)\,\bar{W}\,, \tag{7}$$

where $\bar{W}$ is the uncorrected value. Since no degradation in the instrumental response of the 8-12 micron channel is presumed to exist at the time of launch ($t = 0$), $h_2(0) = 1$. The value of $h_2(t)$ increases throughout the year, reaching 1.250 at the midpoint of period 19 on 5 July 1964.

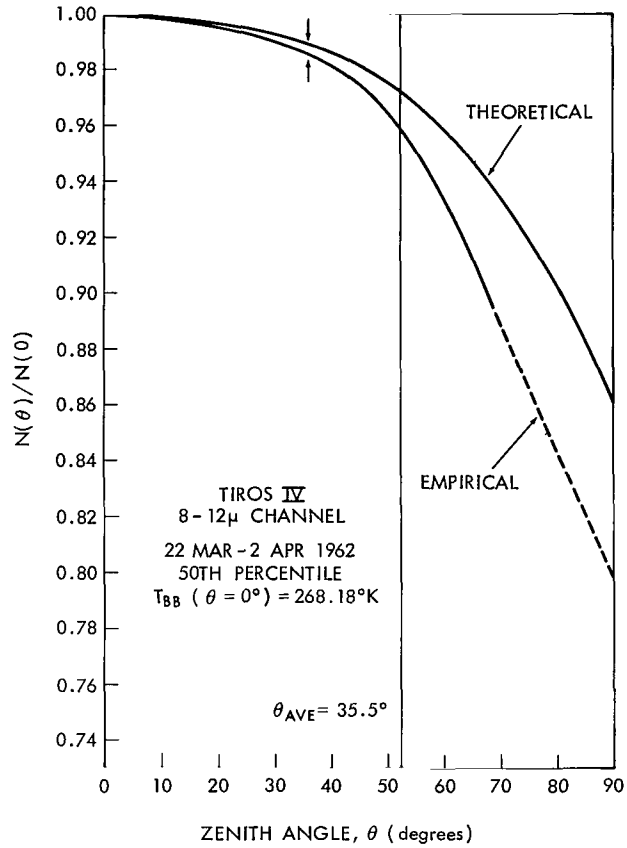

Figure 4—Theoretical vs. empirical limb darkening for the 8-12μ channel of Tiros IV.

Finally the values of total outgoing flux calculated by the computer, W, were corrected manually for (1) instrumental degradation and (2) an empirically determined increase in limb darkening. From Equations 5 and 7 we have for the degradation-corrected value of flux, W',

$$W' = 0.141 + 0.00907\, h_2(t)\,\bar{W}\,. \tag{8}$$

Combining Equations 5 and 8 to eliminate $\bar{W}$, we have

$$W' = h_2(t)\,W - 0.141\,[h_2(t) - 1]\,. \tag{9}$$

Finally from Equations 6 and 9 we have for the outgoing flux, W'', corrected for both instrumental degradation and an empirically determined increase in limb darkening,

$$W'' = 0.986\,\{h_2(t)\,W - 0.141\,[h_2(t) - 1]\} \tag{10}$$

where W is the value of flux calculated by the computer.

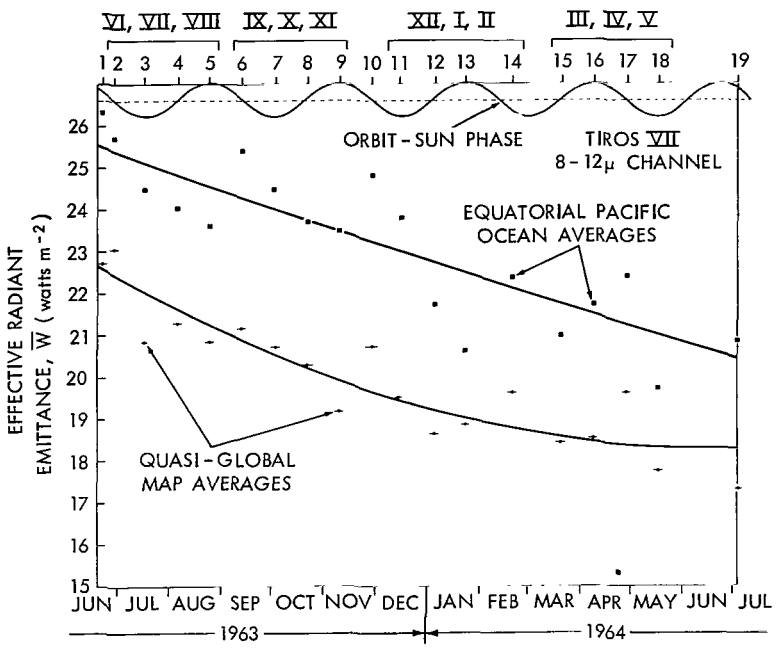

Figure 5—Effective radiant emittances, $\overline{W}$, vs. time from "quasi-global" map averages and equatorial Pacific Ocean averages, indicating a degradation of the instrumental response of the 8-12μ channel of Tiros VII.

Quasi-global averages of reflectances calculated by the computer using Equation 4 from measurements made by the 0.55-0.75 micron channel for each of 17 weekly periods processed during the first year of Tiros VII are shown in Figure 6. Because of an unfavorable orbit-sun geometry, only very small amounts of data were acquired for periods 3 and 13, and these were rejected as being unrepresentative. A least-squares linear curve was calculated for the quasi-global map averages, showing again, a decrease with time. After some comparisons of reflectances calculated over "constant" targets (e.g., the Sahara Desert) for several periods throughout the year, the curve of Figure 6 was adopted as representing the *apparent* degradation of the instrumental response, and was used in determining the factor $h_5(t)$ for correcting the reflectances printed out by the computer. A reflectance value, corrected for apparent instrumental degradation, r_0', becomes

$$r_0' = h_5(t)\, r_0 \,, \tag{11}$$

where r_0 is the uncorrected value.

In initially treating the data using Equations 10 and 11, it was found that the annual planetary albedo required to balance the annual long-wave flux determined from the 8-12 micron channel was 32.2% (cf. "Results" below). On the other hand the annual planetary albedo inferred from values of reflectance calculated by Equation 11 was only 20.1%. If planetary radiative equilibrium exists over one year (and we presume that it very nearly does), there is a glaring inconsistency between the two types of data. There has been a history in the previous Tiros radiometers of abnormally low reflectances and of observed decreases in instrumental response *even before launch* (Refer-

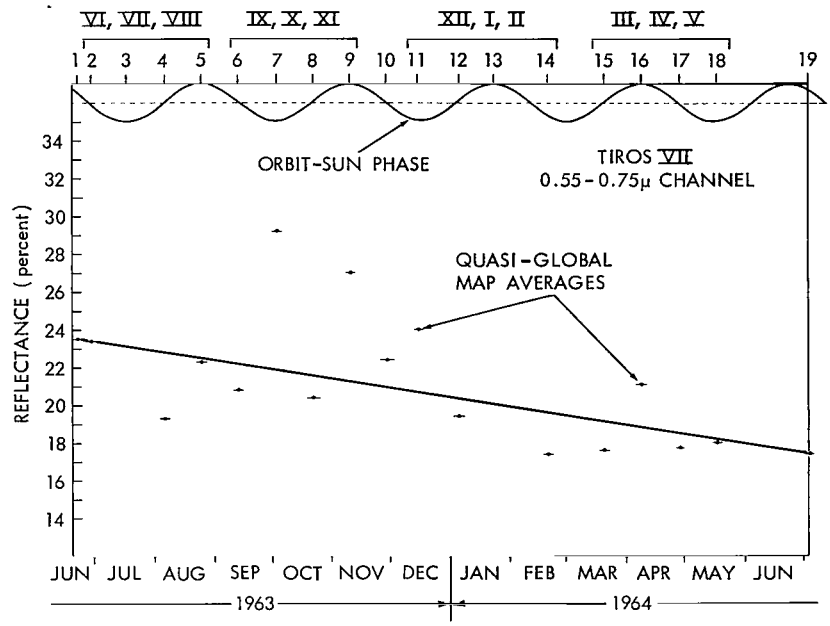

Figure 6—"Quasi-global" map average reflectances vs. time, indicating a degradation of the instrumental response of the 0.55-0.75μ channel of Tiros VII.

ence 13). On the other hand there have been no instances where the long-wave channels were observed to degrade before launch or yield "abnormal" results immediately after launch. Therefore, we shall accept the long-wave fluxes as modified by Equation 10, and multiply the reflectance values, r_0', calculated by Equation 11 by a factor required to satisfy annual radiative equilibrium. This factor is

$$\frac{32.2}{20.1} = 1.60 \tag{12}$$

Finally, from Equations 11 and 12 we have for the reflectances (equivalent to albedo under our assumption of isotropy), corrected for an apparent instrumental degradation and further increased by the factor 1.60 to effect annual planetary radiative equilibrium,

$$r_0'' = \text{albedo} = 1.60\, h_5(t)\, r_0 \,. \tag{13}$$

The additional 1.60 factor is presumed to be due to (1) uncertainties in the backscattered fluxes resulting from not including possible angular dependencies, (2) uncertainties in the original calibration, (3) unobserved deterioration of the instrument between the last check-of-calibration on 5 June 1963 and the first orbit of data on June 19, 1963, (4) the assumption that the reflectance of radiation is independent of wavelength, or (5) some combination of the foregoing. This problem is very puzzling and is under continuing study, but to date no satisfactory explanation has been found.

Zonal averages of the weekly maps were "corrected" in accordance with Equations 10 and 13, and averages from the applicable set of four weekly maps constituted the data for each season.

Meridional integrations were accomplished graphically by means of a planimeter, using "energy diagrams" like those of Figures 7-11 for long-wave and Figure 12 for short-wave radiation.

Results

The final values of outgoing long-wave radiation and albedo are summarized in Table 2.

Table 2

Final Seasonal and Annual Values of Long and Short-Wave Radiation.

Season (Months)	Planetary Long-Wave Radiant Power (10^{15} cal min^{-1})	Solar Radiation (10^{15} cal min^{-1})		Planetary Albedo (%)
		Reflected	Incident on Planet	
J-J-A	1725.2	699.0	2457.8	28.4
S-O-N	1725.2	922.2	2574.8	35.8
D-J-F	1712.2	859.7	2609.8	32.9
M-A-M	1746.5	796.0	2544.2	31.3
Annual	1727.3	819.4	2546.7	32.2

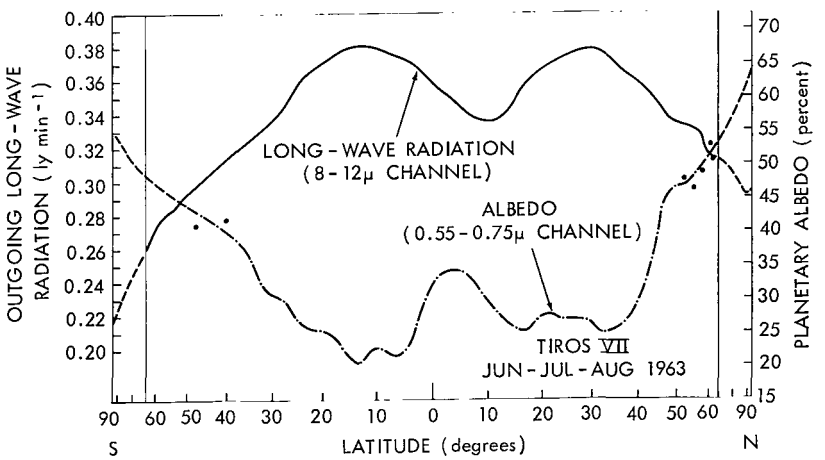

Figure 7—Outgoing long-wave radiation and albedo for June, July, and August 1963. The abscissa is scaled in proportion to zonal areas (sine of the latitude).

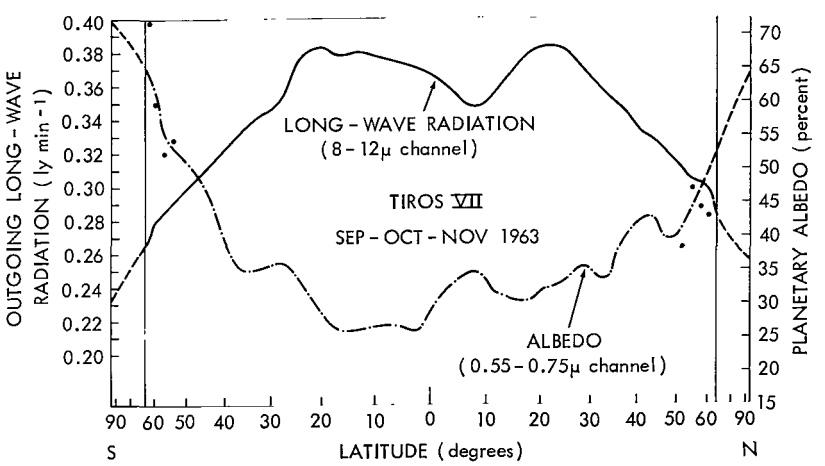

Figure 8—Outgoing long-wave radiation and albedo for September, October, and November 1963. The abscissa is scaled in proportion to zonal areas (sine of the latitude).

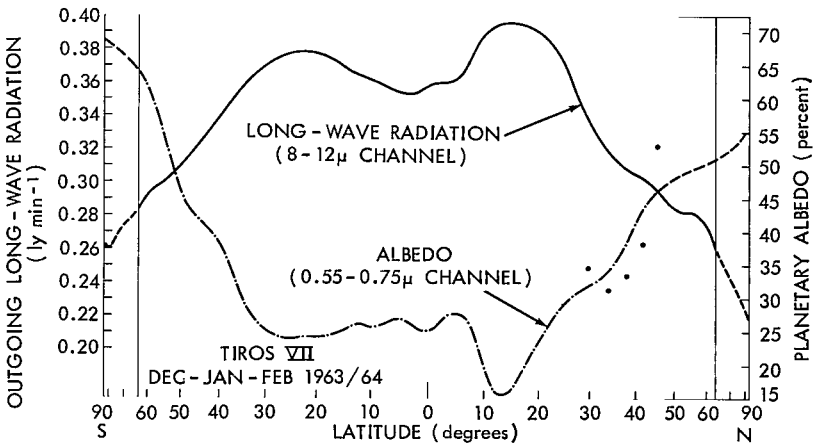

Figure 9—Outgoing long-wave radiation and albedo for December 1963, January, and February 1964. The abscissa is scaled in proportion to zonal areas (sine of the latitude).

Figure 10—Outgoing long-wave radiation and albedo for March, April, and May 1964. The abscissa is scaled in proportion to zonal areas (sine of the latitude).

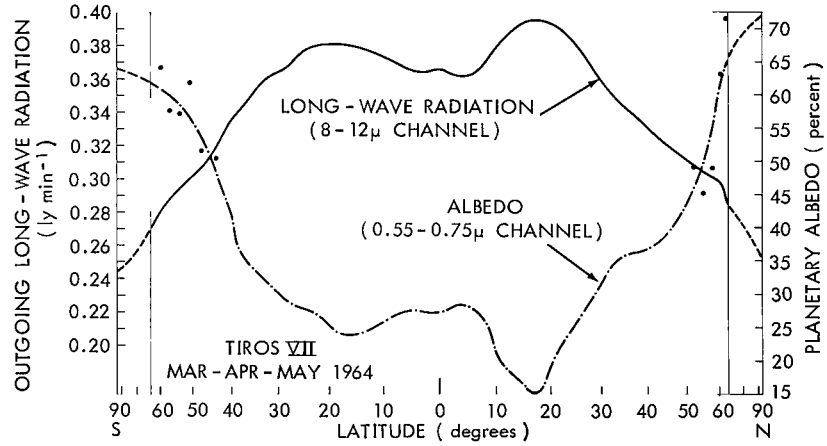

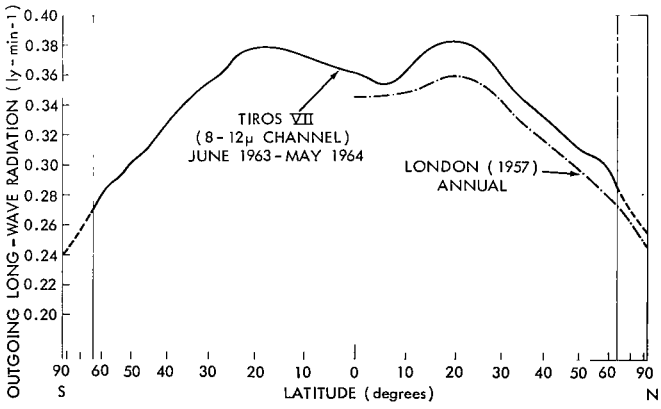

Figure 11—Annual mean outgoing long-wave radiation. The corresponding values of London (1957) for the northern hemisphere are shown for comparison. The abscissa is scaled in proportion to zonal areas (sine of the latitude).

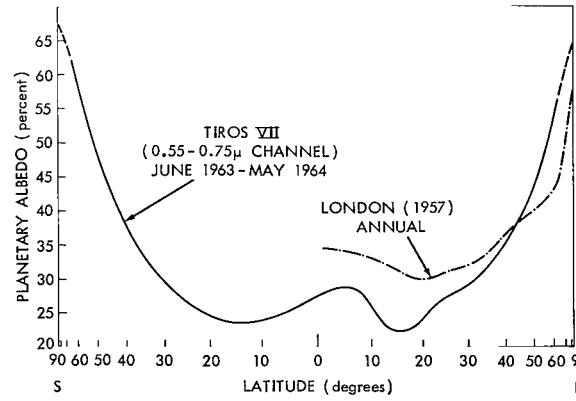

Figure 12—Annual mean planetary albedo. The corresponding values of London (1957) for the northern hemisphere are shown for comparison. The abscissa is scaled in proportion to the annual zonal insolation (top of the atmosphere).

The seasonal values of long-wave radiation and albedo are shown in Figures 7, 8, 9 and 10 and the annual values are shown in Figures 11 and 12. Vertical lines at latitudes 63.5°N. and S. mark the boundaries of the quasi-globe. Dashed lines indicate an extrapolation of the curves beyond (or near) these boundaries where satellite data were not acquired. Dots show the scatter of the short-wave seasonal data at high latitudes where the population of the data samples becomes increasingly smaller. Data from London (Reference 14) are shown in Figures 11 and 12 for comparison.

Two maxima in the long-wave radiation, associated with the subtropical high pressure regions, show up clearly in all figures as does a tropical minimum, associated with the cloudiness of the Intertropical Convergence Zone (ITC). The location of the long-wave tropical minimum remains in the northern hemisphere in all seasons except in December-January-February, clearly pointing up the asymmetry between the hemispheres. Similarly, the long-wave maximum occurs over the subtropical high of the northern hemisphere in all seasons except June-July-August, when the long-wave radiation over the subtropical high in the southern hemisphere becomes only slightly larger. Generally more long-wave radiation is emitted from the extratropical latitudes of the northern hemisphere than from the same latitudes of the southern hemisphere in corresponding seasons. However, in the tropics the situation is reversed where less radiation is emitted from the northern hemisphere than from the southern hemisphere in corresponding seasons. This characteristic tends to equalize the total radiation emitted from the two hemispheres annually. The albedo minimums occur in the tropics of the winter and spring hemispheres but are lowest when they occur in the northern hemisphere.

The tropical annual minimum in the long-wave radiation (and, hence, the approximate mean annual position of the ITC) is located at latitude 5°N, whereas the maximum long-wave radiation is located at latitude 20°N (Figure 11). The emission is smaller in the northern hemisphere between the equator and latitude 15° but larger between latitude 15° and the pole than in the southern hemisphere. The overall long-wave radiation is slightly larger than London's (Reference 14) as would be expected from a comparison of the Tiros-inferred albedo of 32.2% with London's 35.2%.

The tropical maximum in the albedo of Figure 12 occurs at latitude 5°N, consistent with the long-wave minimum, but the minimum albedo occurs at latitude 16°N, slightly south of the position of the long-wave maximum. The albedo in the northern hemisphere generally is larger between the equator and latitude 12° but smaller at higher latitudes than in the southern hemisphere. It is interesting to note the greater meridional gradient of the Tiros-inferred albedo compared to London (Reference 14) in Figure 12. The consequences of this characteristic is a larger required poleward flux of heat across latitude circles.

The maximum poleward flux of heat (Figure 13) is 9.8×10^{16} cal min^{-1} across latitude 36°S, whereas in the northern hemisphere the maximum is only slightly smaller at 9.6×10^{16} cal min^{-1}

across latitude 36° N. A somewhat surprising result is that the poleward flux curve crosses zero near the equator at latitude 0.4°S whereas previous studies by Simpson (Reference 15) placed the crossover at about latitude 4.0°N. The annual curve given by London (Reference 14) is shown for comparison.

The seasonal variations of albedos inferred from Tiros VII are shown in Figure 14. Monthly averages of the stellar magnitudes of measurements of earthlight reflected from the moon made during the years 1926-1935 by Danjon (References 16 and 17) are also plotted. There is an approximate correspondence between the albedo and magnitude ordinates. Danjon found a seasonal minimum in the visual albedo of 32% in July and a maximum of 52% in October. Fritz (Reference 18) pointed out that Danjon's measurements did not include the Pacific Ocean. More recent measurements of this type made by Dzhasybekova, Kazachevskii, and Kharitonov (Reference 19) in the Kazakh SSR during the years 1957-1958 showed considerable variations in the visible albedo (between 31% and 48%) but did not show any clear seasonal fluctuations. However, the data of Figure 14 do seem to give further evidence of a minimum around July and a maximum around October.

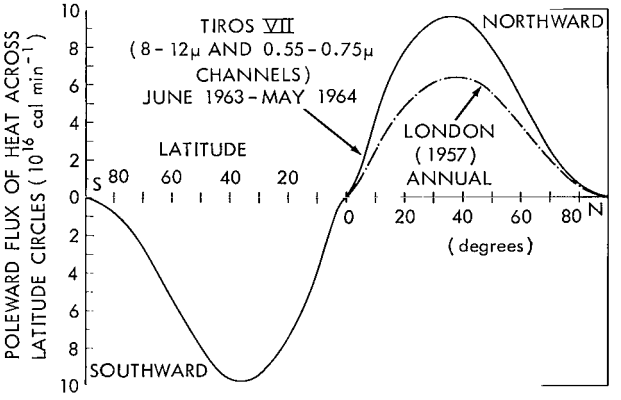

Figure 13—Annual required poleward flux of heat across latitude circles. The corresponding values of London (1957) for the northern hemisphere are shown for comparison.

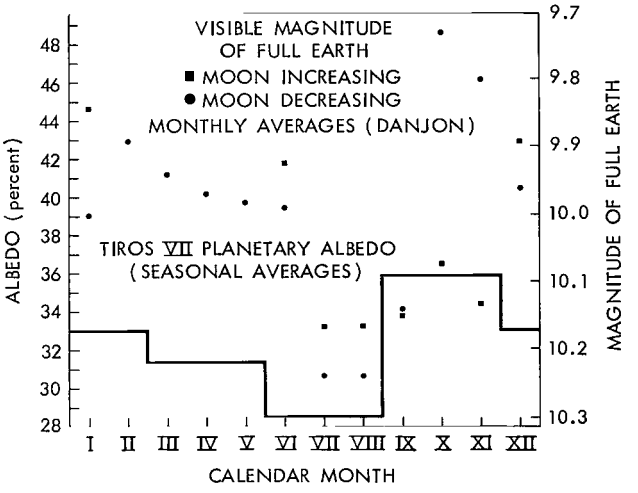

Figure 14—Tiros VII seasonal albedos compared with monthly averages of the magnitudes of earthlight reflected from the moon (after Danjon).

DETERMINATION OF THE MEAN RELATIVE HUMIDITY AND WATER VAPOR MASS OF THE UPPER TROPOSPHERE

Möller (References 20 and 21) developed a method for the determination of the mean relative humidity of the troposphere and of the surface temperature of clouds or of the ground from radiation data of the Tiros meteorological satellites, and Möller and Raschke (Reference 22) have

further developed the method. We shall apply the method to data from the 6-6.5 micron and 8-12 micron channels of Tiros IV during the week 11-18 April 1962, and we shall extend the method to include the inference of the mass of water vapor above 500 mb.

The principle of the method is illustrated in Figure 15. Since approximately the same lapse rate exists in all atmospheres ($\gamma \approx 6.5\,^{\circ}C/km$), and the saturation water vapor pressure is a function only of temperature, it follows that the same water vapor mass exists above the same temperature in all atmospheres having the same relative humidity. The water vapor mass, u, above height, z, can be expressed by

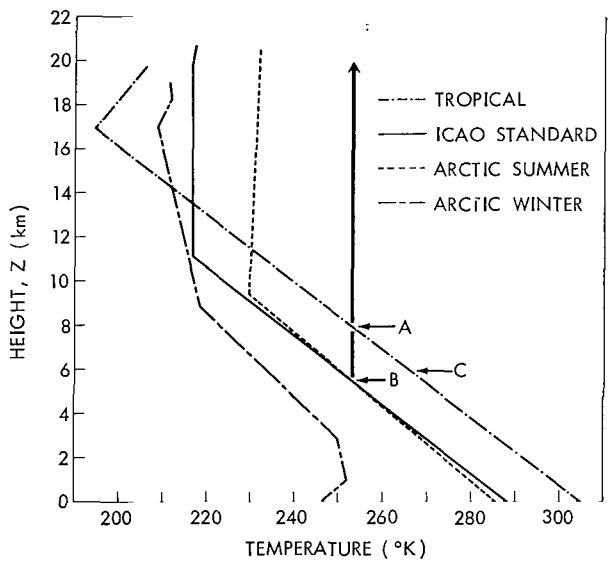

Figure 15—Schematic diagram illustrating that radiation of a given temperature is emitted from approximately the same optical depth in all atmospheres with the same relative humidity (after the method of Möller).

$$u = \int_z^{\infty} \frac{e_s(T(z))\; r(z)}{T(z)\,\frac{R^*}{m_w}}\, dz \qquad (14)$$

where e_s is the saturation water vapor pressure, T is temperature, r is relative humidity, R^* is the universal gas constant, and m_w is the molecular weight of water vapor. Thus in Figure 15, Equation 14 would calculate approximately the same water vapor mass above height A in the tropical atmosphere as it would above height B in the ICAO standard atmosphere for the same relative humidities. The reduced mass of water vapor

$$u^* = \int_0^u \left(\frac{P}{P_0}\right)^n du \qquad (15)$$

which is required for the radiative transfer problem, would be slightly different above the two heights of the previous illustration because of the term $(P/P_0)^n$ which takes into account the pressure broadening of the spectral lines in the absorption band. However, Möller (References 20 and 21) has shown that for the same relative humidity and a lower boundary (ground or cloud) at the same temperature, the outgoing radiance in the interval 6-6.5 microns is nearly the same for all atmospheres. Therefore, to a good approximation one can apply the calculations for one atmosphere to all atmospheres. The evaluation diagram (Figure 16) is designed to determine the mean relative humidity and the surface temperature (of the ground or of clouds) from simultaneous measurements of the 6-6.5 micron channel ("channel 1") and the 8-12 micron channel ("channel 2") (see Reference 21 for a detailed discussion of the construction of the diagram). Figure 16 was constructed for the tropical atmosphere of Figure 15 for Tiros III, using the radiation tables of Elsasser (Reference 23) with a pressure dependence exponent of $n = 1$ in

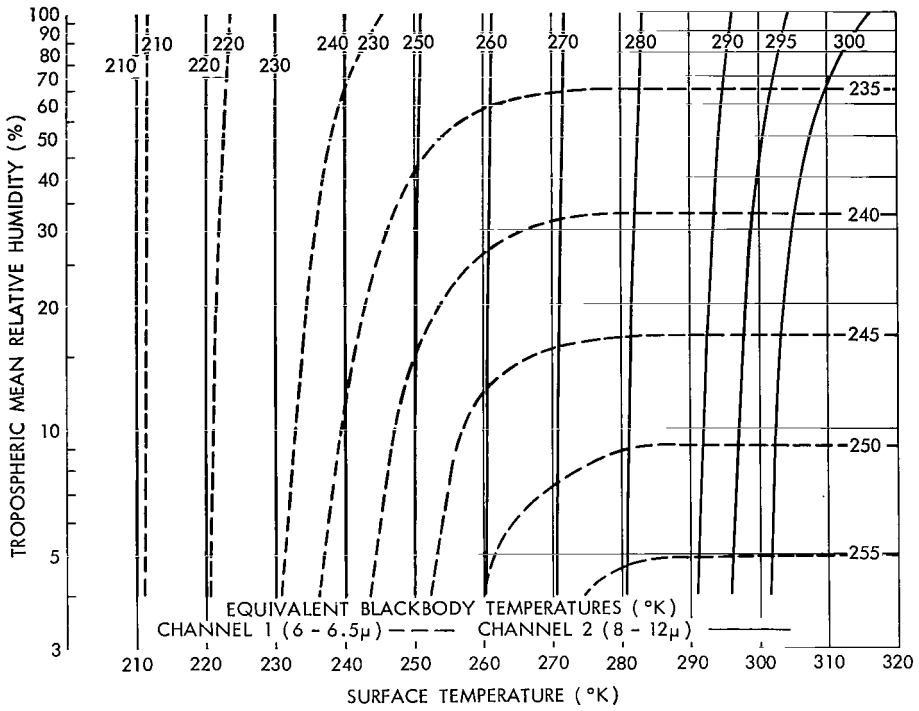

Figure 16—Tiros III evaluation diagram (for determining tropospheric mean relative humidities and surface temperatures of the ground or of clouds).

Equation 15. No attempt was made to "correct" the 6-6.5 micron data, but the 8-12 micron data were corrected for instrumental degradation in accordance with the nomogram given in the Tiros IV Catalog-Manual (Reference 9). The maximum allowable nadir angle was set at 40° to eliminate excessive limb effects. We merely state that the spectral response functions of the 6-6.5 micron and 8-12 micron channels of Tiros III and Tiros IV are very nearly the same as a justification for using the Tiros III diagram with Tiros IV data. Also, the pressure dependence exponent, n, should probably be somewhat less than 1. These items notwithstanding, maps of the 6-6.5 micron and 8-12 micron data of Tiros IV were produced by a computer (similar to the maps used in the heat balance study) for the week 11-18 April 1962, and the conversion to relative humidities was carried out by hand using Figure 16. The resultant "quasi-global" relative humidities are shown in Figure 17

However, if one is interested in the actual water vapor mass, relative humidities can be misleading (i.e., a high relative humidity over the winter arctic may involve much less water vapor than a low relative humidity over the Sahara Desert). To determine the water vapor mass above a given level of a particular atmosphere, having already determined the mean relative humidity, we merely computed the integral of Equation 14 above the temperature in the tropical atmosphere corresponding to the temperature at the given level of the atmosphere in question. For example, suppose that "B" and "C" in Figure 15 are both at the 500 mb levels of their respective atmospheres. Then the water vapor mass above 500 mb in the tropical atmosphere would be determined

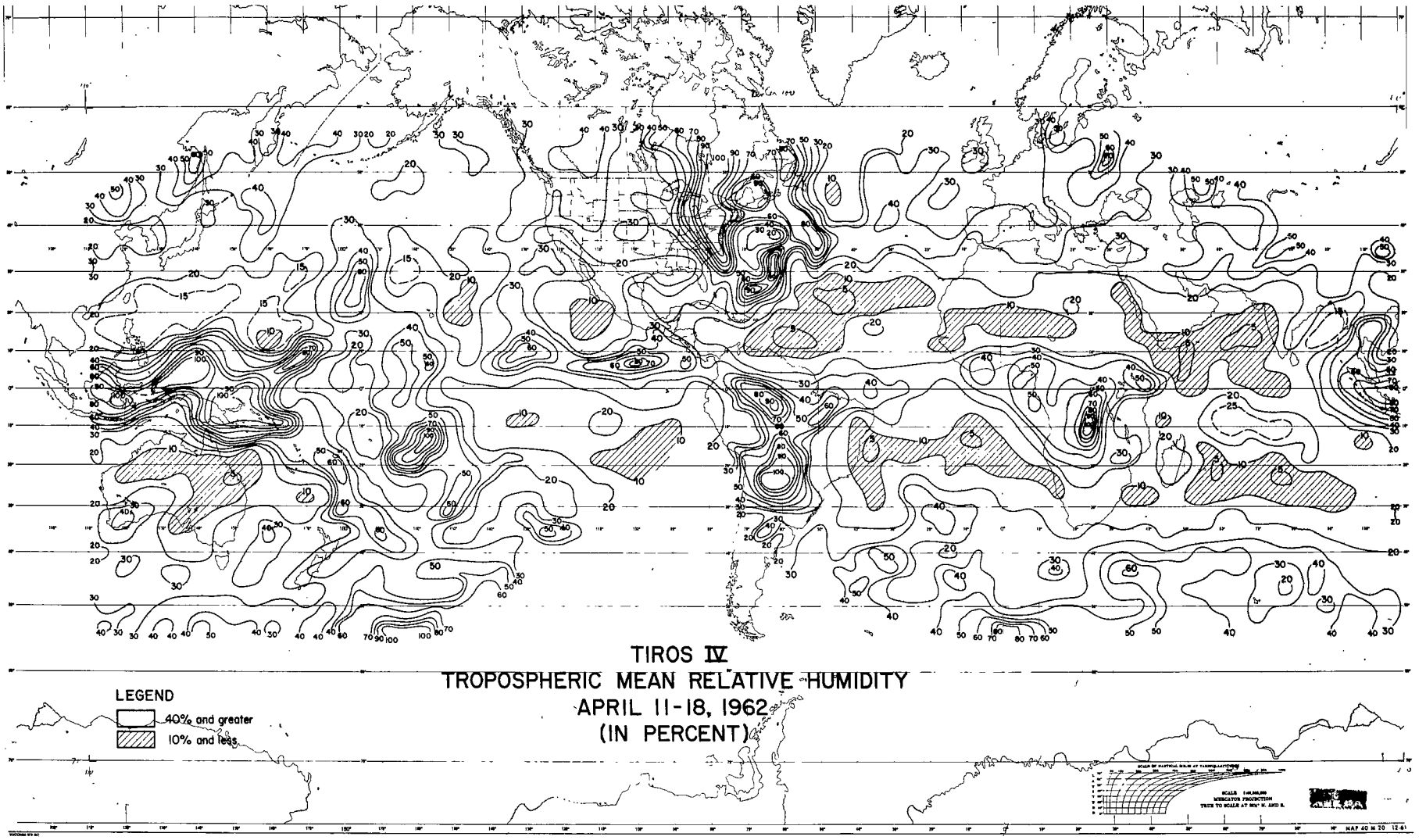

Figure 17—Mean tropospheric relative humidities determined from simultaneous 6.0-6.5 micron and 8-12 micron measurements by Tiros IV during the period 11-18 April 1962, in percent.

by inserting the measured relative humidity in Equation 14 and integrating over the tropical atmosphere from level "C" to infinity. The water vapor mass above 500 mb in the ICAO standard atmosphere would be determined by inserting the measured relative humidity in Equation 14 and integrating over the tropical atmosphere again, but from level "A" (at the same temperature as "B") to infinity. It was decided to make the determination of water vapor mass above 500 mb because the greater part of the radiation sensed by the 6-6.5 micron channel originates above 500 mb (Reference 4) and it was convenient to compare the results with a previous study using conventional data by Bannon and Steele (Reference 24).

A world map of 500 mb temperatures was constructed from radiosonde and climatological data for the week of 11-18 April 1962. Using this map and the relative humidities of Figure 17, calculations of water vapor mass were carried out using the technique described above.

The results of the calculations are shown in Figure 18. The agreement with the results of Bannon and Steele (Reference 24) shown in Figure 19 is generally good. Three major concentrations of water vapor are located over Indonesia, South America, and Africa, comparing favorably both in position and magnitude with Figure 19, although there are smaller included areas of much higher concentrations indicating near-saturation. Two additional indicated moist regions over 6°N, 100°W and 15° S, 160°W (which are not seen in Figure 19) are located near the position of the ITC in April and were found to persist in an analysis of additional data two weeks later. Hence, they too may be semi-permanent in nature, but conclusions cannot be drawn without more extensive analyses. The marked dry tongue over the Sahara Desert extending westward to the Caribbean Sea and the relative dryness everywhere near latitude 20°N, with the consequent decrease in atmospheric absorption and emission, corroborate the long-wave peak near this latitude in Figure 10. Considering the many approximations used, it is not possible at this time to fully assess the validity of the results, but the patterns are encouraging for additional work in this area.

MEASUREMENT OF STRATOSPHERIC TEMPERATURES

One of the optical channels of the Tiros VII radiometer measured infrared radiation emitted mainly by carbon dioxide in the earth's atmosphere at wavelengths ranging from 14.8 to 15.5 microns. A detailed discussion of the physical significance of the measurements in this spectral interval and of the temperature patterns mapped during the first nine months of Tiros VII has been given by Nordberg et al. (Reference 25). We shall only demonstrate by a few examples the ability of this channel to map the mean temperatures of the lower stratosphere on a global scale, and we refer the reader to the original paper for a complete discussion.

The outgoing effective radiance, $\bar{N}$, in the direction of the satellite can be expressed by

$$\bar{N} = \frac{1}{\pi} \int_{\lambda=0}^{\infty} \int_{z=0}^{\infty} B_\lambda(T(z))\ \phi_\lambda \frac{\partial \tau_\lambda(z)}{\partial z}\ dz\ d\lambda\ , \qquad (16)$$

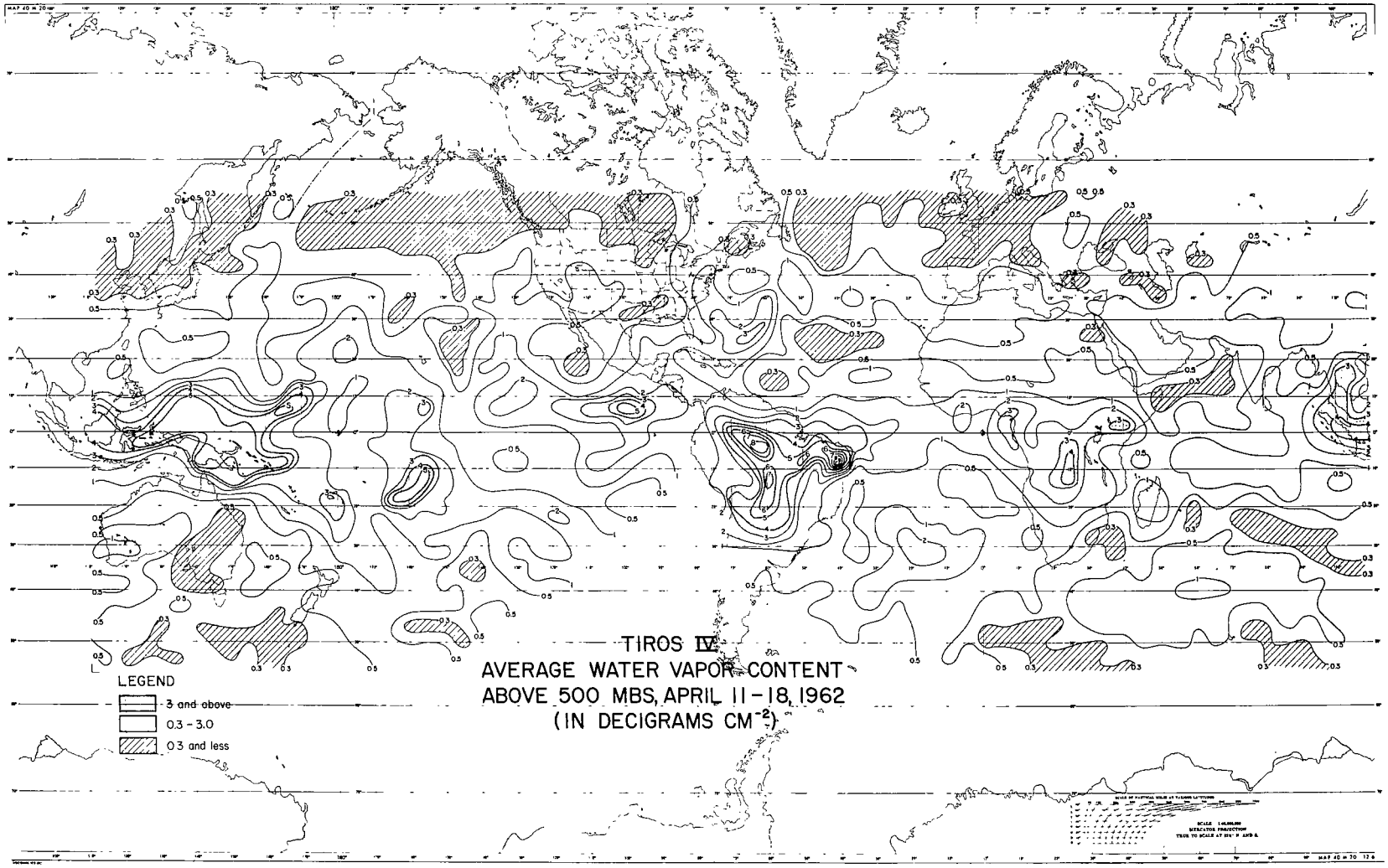

Figure 18—Average water vapor content above 500 mb determined from simultaneous 6.0-6.5 micron and 8-12 micron measurements by Tiros IV and 500 mb temperatures from radiosonde data during the period 11-18 April 1962, in decigrams cm^{-2}.

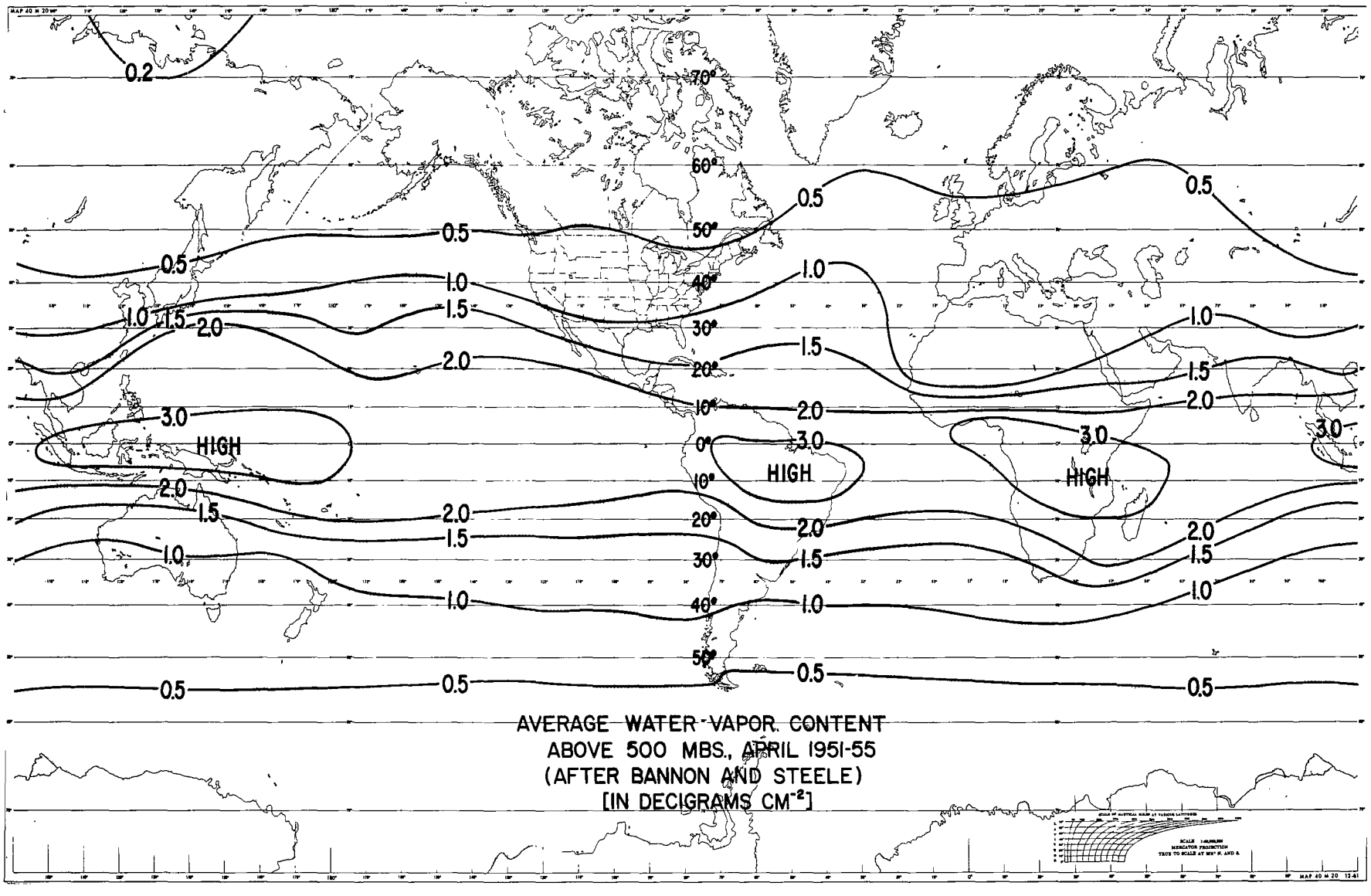

Figure 19—Average water vapor content above 500 mb, April 1951-55, in decigrams cm^{-2}. (After Bannon and Steele).

which can be simplified to read

$$\bar{N} = \frac{1}{\pi} \int_{z=0}^{\infty} \psi(z)\, dz \,, \tag{17}$$

where

$$\psi(z) = \int_{\lambda=0}^{\infty} B_\lambda(T(z))\, \phi_\lambda \frac{\partial \tau_\lambda(z)}{\partial z}\, d\lambda \,, \tag{18}$$

and

B = Planck function (flux),

ϕ_λ = spectral response function of channel,

τ = atmospheric beam transmittance in the direction of the satellite

z = height above the surface.

The spectral response function of the channel is shown in Figure 20. Four model atmospheres are shown in Figure 21(a). A homogeneous distribution of CO_2 of 0.00031 fractional parts by volume was assumed in the atmosphere. Using the radiation tables of Elsasser (Reference 23) and a pressure-dependence exponent of $n = 1$, the $\psi(z)$ functions for the four model atmospheres were computed for nadir angles of 0° and 58° (equivalent to a zenith angle of 69°) and plotted in Figures 21(b) and (c). From Figure 21 it may be seen that about 65 percent of the integrated radiance reaching the satellite originates in the region from 15 to 35 km for a nadir angle of 0° and that the weighting curves are shifted upward about 2.5 km for a nadir angle of 58°. Thus even though there are contributions from higher and lower layers, it is seen that the measurements may primarily be interpreted in terms of temperatures of the lower stratosphere.

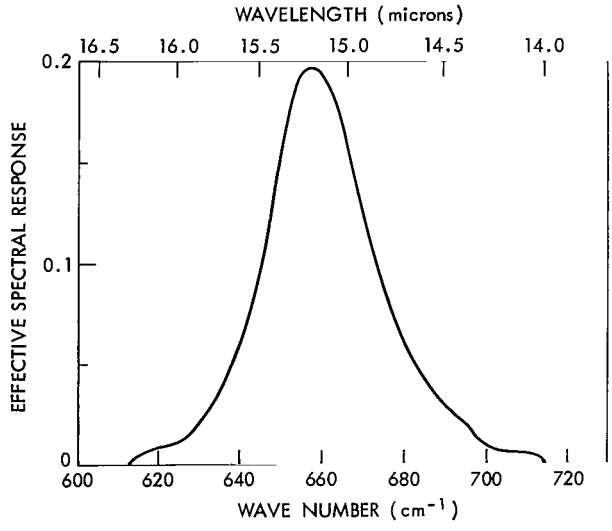

Figure 20—Effective spectral response of the Tiros VII 15μ channel as a function of wavelength.

A typical temperature pattern at the start of the northern hemisphere summer and southern hemisphere winter is shown in Figure 22. Stratospheric mean temperatures averaged over the week immediately after the launch of Tiros VII, 19-25 June 1963, range from 240°K near latitude 60°N to 215°K near 60°S. The generally zonal structure of the temperature pattern confirms the established knowledge of the lower stratosphere, namely, the existence of a very strong cyclonic circulation system around the cold low pressure core centered near the winter

pole and an anticyclonic circulation system around the warm high pressure system centered over the summer pole.

The map for the period 25 September - 1 October 1963 illustrates the transition period. It is important to point out that due to instrumental degradation, all temperatures shown in Figure 23 and in all succeeding maps are about 7°K too low, inasmuch as the degradation seemingly leveled off in July and August after an initial rather rapid decline. In Figure 23 the southern winter vortex has broken down and the temperature gradients between the two hemispheres have reached their minimum during the transition period.

The map for the period 15-22 January 1964 (Figure 24) illustrates the state of the stratosphere in opposite seasons to those depicted in Figure 22. The southern hemisphere summer pattern is very much like its northern hemisphere counterpart in Figure 22. However, a striking difference is seen in the northern hemisphere winter. The "Aleutian Anticyclone", a regular climatological feature, displaces the cold stratospheric cyclone from the position of symmetry

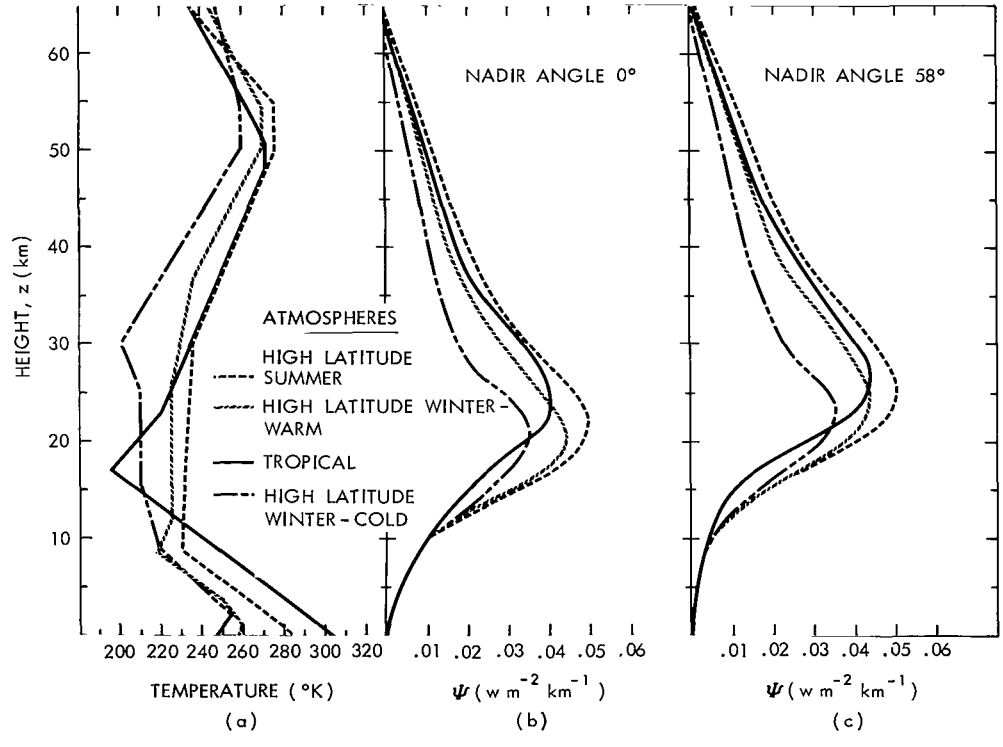

Figure 21(a)—Typical temperature profiles based on proposed supplements to the "U. S. Standard Atmosphere 1962" for 60° North summer, 60° North winter (warm and cold) and 15° North. The "warm" and "cold" temperature profiles for 60° N ("high latitude winter") can be considered typical at these latitudes depending on the state of the stratosphere in these regions; (b) Weighting functions ψ (z), applying to the measured outgoing radiance $\overline{N}$ (nadir angle = 0°); (c) Weighting functions ψ (z), applying to the measured outgoing radiance $\overline{N}$ (nadir angle = 58°).

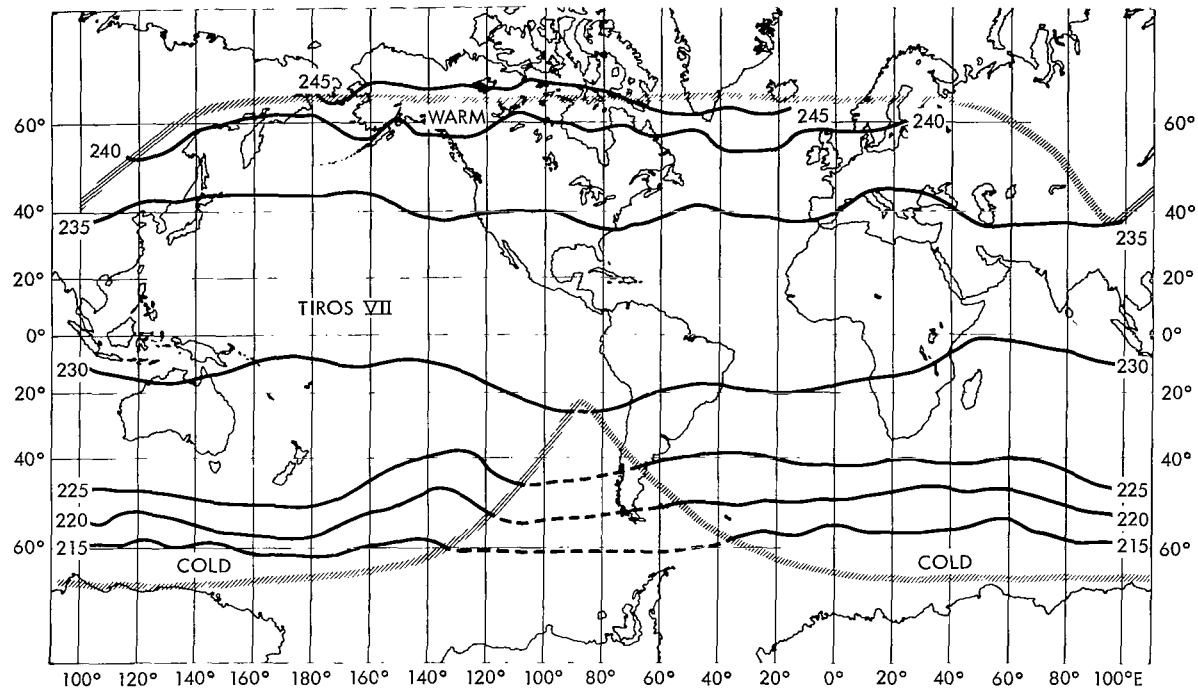

Figure 22—Quasi-global map of 15μ equivalent blackbody temperatures averaged over the week 19-25 June 1963 (nadir angle 0°-40°).

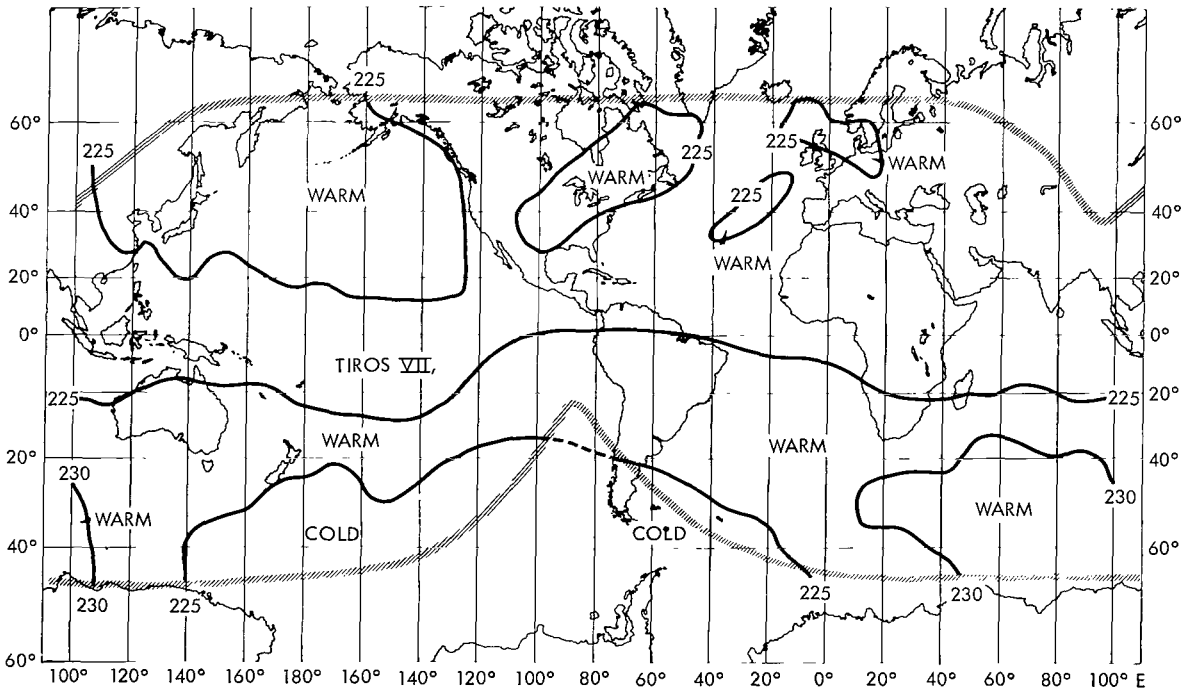

Figure 23—Quasi-global map of 15μ equivalent blackbody temperatures averaged over the week 25 September-1 October 1963 (nadir angle 0°-40°).

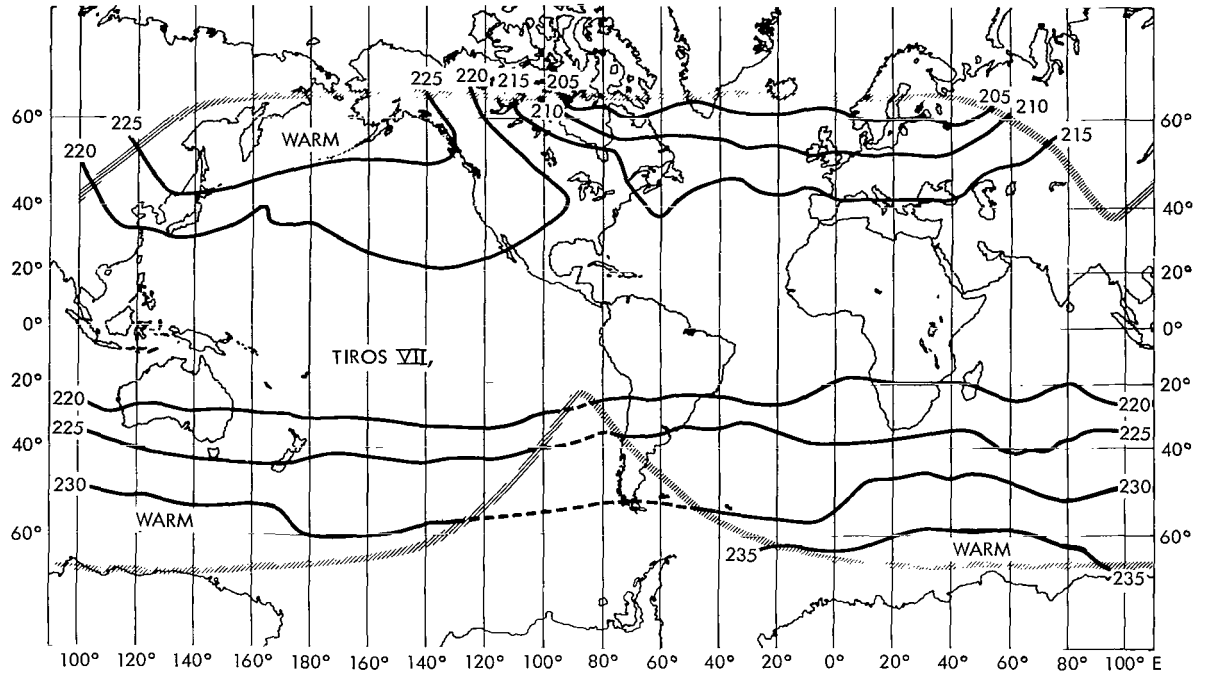

Figure 24—Quasi-global may of 15μ equivalent blackbody temperatures averaged over the week of 15-22 January 1964 (nadir angle 0°-40°).

that one might expect it to have. The strong Aleutian Anticyclone established itself in the first week of December and remained throughout the entire winter.

During the last week of January 1964 a stratospheric warming of apparently moderate intensity occurred over the region of the Caspian Sea. The situation is summarized in Figure 25 which shows that on 27 January the radiation temperatures had increased by 15°K over the averages for the week of 9-15 January near the center. During the following week, 31 January-8 February, the warming passed its climax and dissipated soon thereafter.

The global temperature structure undergoes a major change during the period from early February to the period around the Vernal Equinox in Figure 26. The strong zonal winter temperature patterns, particularly over the eastern hemisphere, as well as the zonal summer pattern in the southern hemisphere have disappeared. The southern hemisphere has cooled considerably, resulting again, as in September, in an almost constant temperature, 223° + 7°K, prevailing over the entire globe.

SUMMARY

Studies involving satellite radiometric data have been carried out in three areas of climatological interest—the planetary heat balance, the upper tropospheric content and distribution of

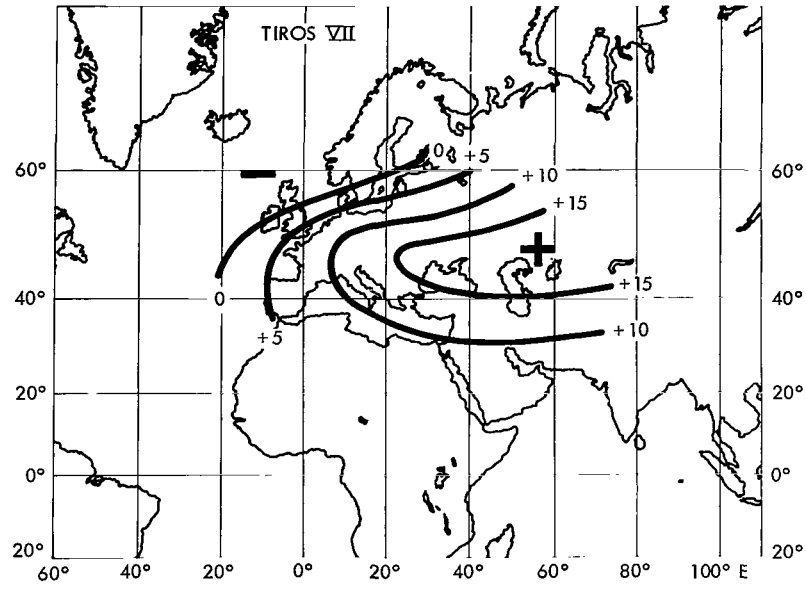

Figure 25—Regional map of the differences between the 15μ equivalent blackbody temperatures measured on 27 January 1964 and those averaged over the week 9-15 January (nadir angle 0°-40°). The effects of a stratospheric warming over Eastern Europe are illustrated.

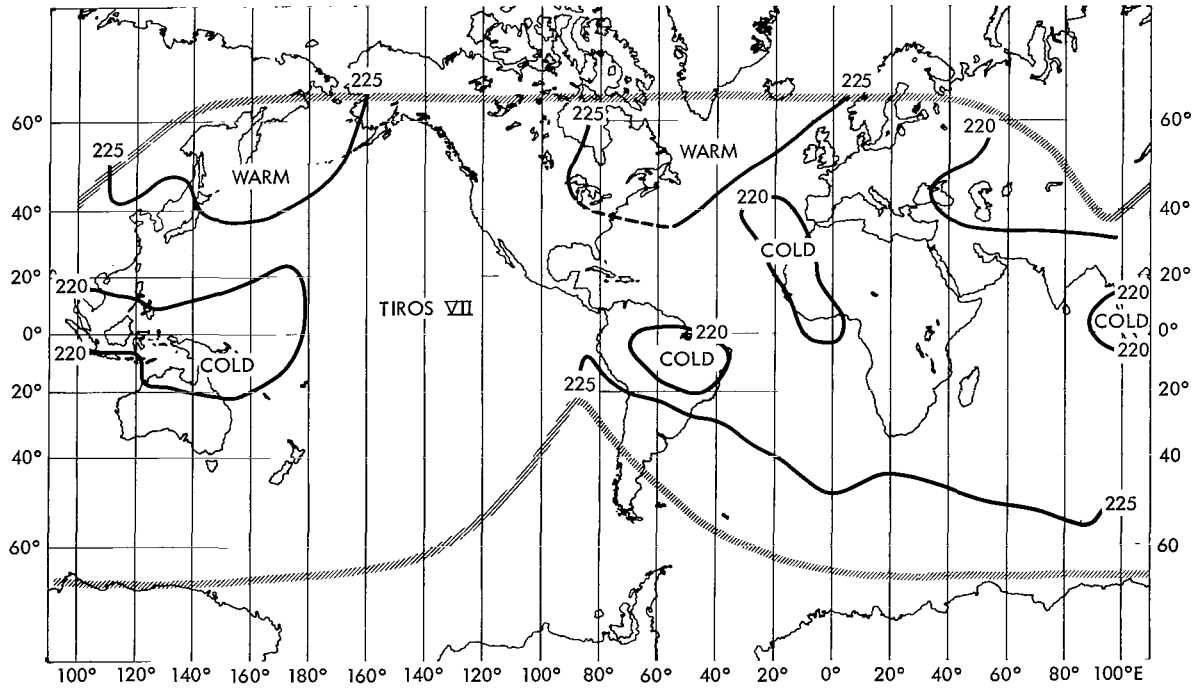

Figure 26—Quasi-global map of 15μ equivalent blackbody temperatures averaged over the week 18-25 March 1964 (nadir angle 0°-40°).

water vapor, and the temperature and associated circulation patterns of the lower stratosphere. Even though difficulties exist in certain areas, such as instrumental stability, and interpretations of the essentially-beam measurements, the results give a new insight into the large-scale, long-term radiative characteristics of our planet and the physical processes which can be derived from them. The comparative relationships indicating hemispheric asymmetries and seasonal fluctuations in the various parameters appear to be valid.

Finally, the potentialities of climatological investigations from future satellites–in polar orbits and with improved instrumentation–have been clearly demonstrated, we believe, by the studies reported in this paper.

ACKNOWLEDGMENTS

We gratefully acknowledge the contributions of the many persons who have contributed to the success of the Tiros series of meteorological satellites. We are particularly indebted to Mr. Robert Hite and his associates for their computational efforts in reducing the vast amount of radiation measurements and to Mr. Lewis Allison for his significant contributions in regard to the water vapor analyses.

(Manuscript received November 2, 1964)

REFERENCES

1. Bandeen, W. R., Hanel, R. A., Licht, J., Stampfl, R. A., and Stroud, W. G., "Infrared and Reflected Solar Radiation Measurements from the Tiros II Meteorological Satellite," *J. Geophys. Res.* 66(10):3169-3185, October 1961.
2. Nordberg, W., Bandeen, W. R., Conrath, B. J., Kunde, V., and Persano, I., "Preliminary Results of Radiation Measurements from the Tiros III Meteorological Satellite," *J. Atmos. Sci.* 19(1):20-30, January 1962.
3. Kondrat'ev, K. IA., "Meteorologicheskie Sputniki," Leningrad: Hydrometeorological Publishing House, 1963 (In Russian).
4. Hanel, R. A., and Wark, D. Q., "Tiros II Radiation Experiment and its Physical Significance," *J. Opt. Soc. Am.* 51(12):1394-1399, December 1961.
5. Fritz, S., and Winston, J. S., "Synoptic Use of Radiation Measurements from Satellite Tiros II," *Month. Weather Rev.* 90(1):1-9, January 1962.
6. Bandeen, W. R., Kunde, V., Nordberg, W., and Thompson, H. P., "Tiros III Meteorological Satellite Radiation Observations of a Tropical Hurricane," *Tellus* 16(4) Oct.-Dec. 1964 (in press).
7. Staff members, "Tiros II Radiation Data Users' Manual," Washington: U. S. Weather Bureau, U. S. Dept. of Commerce, and National Aeronautics and Space Administration, August 15, 1961.

8. Staff members, "Tiros III Radiation Data Users' Manual," Washington: National Aeronautics and Space Administration, August 1962.

9. Staff members, "Tiros IV Radiation Data Catalog and Users' Manual," Washington: National Aeronautics and Space Administration, 1963.

10. Staff members, "Tiros VII Radiation Data Catalog and Users' Manual," Volume 1, Washington: National Aeronautics and Space Administration, 1964 (in press).

11a. Wark, D. Q., Yamamoto, G., and Lienesch, J. H., "Methods of Estimating Infrared Flux and Surface Temperature from Meteorological Satellites," *J. Atmos. Sci.* 19(5):369-384, September 1962.

11b. Wark, D. Q., Yamamoto, G., and Lienesch, J., "Infrared Flux and Surface Temperature Determinations from Tiros Radiometer Measurements," Washington: U. S. Weather Bureau, Meteorological Satellite Laboratory, MSL Rept. 10 and Supplement; N63-11881, August 1962, 1963.

12. Staff members, "Tiros III Radiation Data Catalog," Washington: U. S. Weather Bureau, U. S. Dept. of Commerce, and National Aeronautics and Space Administration, 1962.

13. Bandeen, W. R., Samuelson, R. E., and Strange, I., "Tiros III Radiation Data Users' Manual Supplement - Correction Models for Instrumental Response Degradation," Washington: National Aeronautics and Space Administration, 1963.

14. London, J., "A Study of the Atmospheric Heat Balance," Final Report, New York, New York University College of Engineering, Dept. of Meteorology and Oceanography, AFCRC TR-57-287; AD-117 227, July 1957.

15. Simpson, G. C., "Distribution of Terrestrial Radiation," *Roy. Meteorol. Soc. Mem.* 3(23):53-78, April 1929.

16. Danjon, A., "Nouvelles Recherches sur la Photométrie de la Lumière Cendrée et l'Albedo de la Terre," *Strasbourg Univ. Observat. Ann.* 3(3):139-180, (1936).

17. Danjon, A., "Albedo, Color, and Polarization of the Earth," In: "The Solar System. The Earth as a Planet," Vol. 2 (G. P. Kuiper, ed.): 726-738, Chicago: University of Chicago Press, 1954.

18. Fritz, S., "The Albedo of the Planet Earth and of Clouds," *J. Meteorol.* 6:277-282, August 1949.

19. Dzhasybekova, E. K., Kazachevskii, V. M., and Kharitonov, A. V., "Determination of the Earth's Albedo," *Astron. Zh.* 37(1):131-134, 1960. (In Russian); transl. in: *Soviet Astron. AJ,* 4(1):125-128, July-August 1960.

20. Möller, F., "Atmospheric Water Vapor Measurements at 6-7 Microns from a Satellite," *Planet. Space Sci.* 5:202-206, July 1961.

21. Möller, F., "Einige Vorläufige Auswertungen der Strahlungsmessungen von Tiros II," *Arch. Meteorol. Geophys. Bioklimatol.* Ser. B, 12(1):78-94, July 1962.

22. Möller, F., and Raschke, E., "Evaluation of Tiros III Radiation Data," Contractor Report CR-112, Washington: National Aeronautics and Space Administration, 1964.

23. Elsasser, W. M., and Culbertson, M. F., "Atmospheric Radiation Tables," *Meteorol. Monographs* 4(23):1-43, August 1960.

24. Bannon, J. K., and Steele, L. P., "Average Water-Vapour Content of the Air," *Gt. Brit. Meteorol. Off. Geophys. Mem.* 13(102):1-38, 1960.

25. Nordberg, W., Bandeen, W. R., Kunde, V., and Warnecke, G., "Stratospheric Temperature Patterns Based on Radiometric Measurements from the TIROS VII Satellite," in: "Space Research V,": Proceedings of the 5th International Space Science Symposium, Florence, Italy, May 1964. Amsterdam: North-Holland Publishing Co., in press, 1965.

Appendix A

List of Symbols

γ	Atmospheric lapse rate (°C/km)
ζ	Solar zenith angle
θ_{ave}	Average scan zenith angle
ρ_λ	Spectral reflectivity of calibrating white surface (ideally diffuse or Lambertian)
τ	Atmospheric beam transmittance in the direction of the satellite
ϕ_λ	Effective spectral response function for a radiometer channel
B_λ	Planck function (flux) at wavelength λ
e_s	Saturation water vapor pressure
$h_2(t)$	Correction factor for degradation in response of 8-12 micron channel
$h_5(t)$	Correction factor for degradation in response of 0.55-0.75 micron channel
J_λ	Spectral radiant intensity of calibrating light source (watts $ster^{-1}$ $micron^{-1}$)
m_w	Molecular weight of water vapor
$\overline{N}$	Effective radiance to which a sensor responds (watts m^{-2} $ster^{-1}$)
N'	Arbitrary radiance
n	Pressure dependence exponent
P	Actual atmospheric pressure
P_0	Atmospheric standard surface pressure (1013.25 mb)
R	Calibration distance (meters) between standard lamp and diffuse reflecting surface in laboratory calibration of 0.55-0.75 micron channel
R_a	Distance from earth to sun in astronomical units
R*	Universal gas constant
r	Relative humidity
r_0	Reflectance of solar radiation
r_0'	Reflectance corrected for apparent instrumental degradation
r_0''	Reflectance r_0', further increased by the factor 1.60 (see Equation 13)
S_λ	Spectral irradiance of earth by sun at distance of one astronomical unit

T	Temperature ($^{\circ}K$)
T_{BB}	Equivalent blackbody temperature ($^{\circ}K$)
u	Water vapor mass
u^*	Reduced mass of water vapor
W	Total outgoing long-wave flux (langleys min^{-1})
$W_\lambda(T_{BB})$	Spectral radiant emittance (Planck radiation) from a blackbody at temperature T_{BB}
W'	Degradation-corrected value of outgoing flux W
W''	Outgoing flux W', further corrected for an empirically-determined increase in limb darkening (see Equation 10)
$\overline{W}$	Effective radiant emittance to which a sensor responds (watts m^{-2})
$\overline{W}^*$	Effective solar constant (watts m^{-2})
$\overline{W}'$	Degradation-corrected value of $\overline{W}$
z	Arbitrary height above earth's surface

"The aeronautical and space activities of the United States shall be conducted so as to contribute . . . to the expansion of human knowledge of phenomena in the atmosphere and space. The Administration shall provide for the widest practicable and appropriate dissemination of information concerning its activities and the results thereof."

—NATIONAL AERONAUTICS AND SPACE ACT OF 1958

NASA SCIENTIFIC AND TECHNICAL PUBLICATIONS

TECHNICAL REPORTS: Scientific and technical information considered important, complete, and a lasting contribution to existing knowledge.

TECHNICAL NOTES: Information less broad in scope but nevertheless of importance as a contribution to existing knowledge.

TECHNICAL MEMORANDUMS: Information receiving limited distribution because of preliminary data, security classification, or other reasons.

CONTRACTOR REPORTS: Technical information generated in connection with a NASA contract or grant and released under NASA auspices.

TECHNICAL TRANSLATIONS: Information published in a foreign language considered to merit NASA distribution in English.

TECHNICAL REPRINTS: Information derived from NASA activities and initially published in the form of journal articles.

SPECIAL PUBLICATIONS: Information derived from or of value to NASA activities but not necessarily reporting the results of individual NASA-programmed scientific efforts. Publications include conference proceedings, monographs, data compilations, handbooks, sourcebooks, and special bibliographies.

Details on the availability of these publications may be obtained from:

SCIENTIFIC AND TECHNICAL INFORMATION DIVISION

NATIONAL AERONAUTICS AND SPACE ADMINISTRATION

Washington, D.C. 20546